ARL-TR-10006 ● Oct 2024

Compact Designer Detectors Based on 2D-Plexcitonic Heterostructures

by Ibrahim Boulares, Christopher T Kuhs, Matthew L Chin, Mahesh Neupane, Philip Kim, Jue Wang, Nadine Leisgang, Robert J Boyd, Daniel Rhodes, Henry O Everitt, Sina Najmaei, and Blair C Connelly

NOTICES

Disclaimers

The findings in this report are not to be construed as an official Department of the Army position unless so designated by other authorized documents.

Citation of manufacturer's or trade names does not constitute an official endorsement or approval of the use thereof.

Destroy this report when it is no longer needed. Do not return it to the originator.

ARL-TR-10006 ● OCT 2024

Compact Designer Detectors Based on 2D-Plexcitonic Heterostructures

Ibrahim Boulares, Christopher T Kuhs, Matthew L Chin, Mahash Neupane, Henry O Everitt, Sina Najmaei, and Blair C Connelly
DEVCOM Army Research Laboratory

Philip Kim, Jue Wang, and Nadine Leisgang
Harvard University

Robert J Boyd and Daniel Rhodes
University of Wisconsin-Madison

REPORT DOCUMENTATION PAGE

1. REPORT DATE	2. REPORT TYPE	3. DATES COVERED	
		START DATE	END DATE
October 2024	Technical Report	October 1, 2022	September 30, 2023

4. TITLE AND SUBTITLE
Compact Designer Detectors Based on 2D-Plexcitonic Heterostructures

5a. CONTRACT NUMBER	5b. GRANT NUMBER	5c. PROGRAM ELEMENT NUMBER
5d. PROJECT NUMBER	**5e. TASK NUMBER**	**5f. WORK UNIT NUMBER**

6. AUTHOR(S)
Ibrahim Boulares, Christopher T Kuhs, Matthew L Chin, Mahesh Neupane, Philip Kim, Jue Wang, Nadine Leisgang, Robert J Boyd, Daniel Rhodes, Henry O Everitt, Sina Najmaei, and Blair C Connelly

7. PERFORMING ORGANIZATION NAME(S) AND ADDRESS(ES)	8. PERFORMING ORGANIZATION REPORT NUMBER
DEVCOM Army Research Laboratory ATTN: FCDD-RLA-PE Adelphi, MD 20783	ARL-TR-10006

9. SPONSORING/MONITORING AGENCY NAME(S) AND ADDRESS(ES)	10. SPONSOR/MONITOR'S ACRONYM(S)	11. SPONSOR/MONITOR'S REPORT NUMBER(S)

12. DISTRIBUTION/AVAILABILITY STATEMENT
DISTRIBUTION STATEMENT A. Approved for public release: distribution unlimited.

13. SUPPLEMENTARY NOTES
ORCIDs: Ibrahim Boulares, 0000-0001-7252-4792; Christopher T Kuhs, 0000-0002-3168-1836; Matthew L Chin, 0000-0002-1637-2242; Philip Kim, 0000-0002-8255-0086; Jue Wang, 0000-0001-6843-9771; Nadine Leisgang, 0000-0002-6612-866X; Daniel Rhodes, 0000-0002-7651-3211; Henry O Everitt, 0000-0002-8141-3768; Sina Najmaei, 0000-0003-4650-1997

14. ABSTRACT
Realization of disruptive technological breakthroughs requires investigating fundamentally different materials than those currently employed, as well as utilizing advanced physical properties and device architectures. Emerging 2D van der Waals heterostructures show promise for devices with unprecedented levels of tunability through the 0.75–2.00 eV spectral range, as well as functionality through using different layer thicknesses, stacking configurations, and chemical modifications. To exploit these properties, we investigated the basic physical interactions in heterogeneously stacked 2D transition-metal dichalcogenides (TMDs) with plasmonic nanoparticles that can be exploited for advanced optoelectronic devices. Our efforts demonstrated room-temperature interlayer excitons in TMDs and plasmonic coupling between gold nanocubes and a TMD monolayer. Additionally, we investigated lithography techniques for pattering plasmonic arrays onto TMD monolayers. Finally, we used computational modeling to examine the band structure of TMD heterostructures to predict a device's optical properties and compare them with future experiments. This effort aims to pioneer the development of hybrid 2D TMD plasmonic-nanoparticle excitonic, or "plexcitonic," devices for transformational high-speed, low-energy optoelectronics. By tailoring a plexcitonic device's material properties, using engineered stacking configurations and plasmonic couplings, we will gain unprecedented control of device performance. This will benefit remote and distributed sensing applications with orders-of-magnitude improvement in size, weight, and power and device responsivities.

15. SUBJECT TERMS
spectroscopy; plexcitonics; 2D materials; transition metal dichalcogenides; excitons; Photonics, Electronics, and Quantum Sciences

16. SECURITY CLASSIFICATION OF:			17. LIMITATION OF ABSTRACT	18. NUMBER OF PAGES
a. REPORT	b. ABSTRACT	C. THIS PAGE		
UNCLASSIFIED	UNCLASSIFIED	UNCLASSIFIED	UU	41

19a. NAME OF RESPONSIBLE PERSON	19b. PHONE NUMBER *(Include area code)*
Christopher T Kuhs	christopher.t.kuhs.civ@army.mil

STANDARD FORM 298 (REV. 5/2020)
Prescribed by ANSI Std. Z39.18

Contents

List of Figures iv

List of Tables vi

1. Introduction 1

2. Project Overview 3

3. Modeling of Excitons in TMDs 5

4. Material Development 9

5. Spectroscopy and TMD Analysis 13

6. Plasmonic Coupling to TMDs 20

7. Conclusion: ARL's 2D Material-to-System Integration Roadmap 24

8. References 27

List of Symbols, Abbreviations, and Acronyms 31

Distribution List 33

List of Figures

Fig. 1 (a) Plasmonic nanoparticle on TMD.[9] (b) Stacked TMD excitonic device. (c) Energy band diagram of targeted TMD layer stacks for three candidate heterostructures (adapted from Durán Retamal et al.[10]), chosen based on effective mass (m*) mismatch and staggered band alignment, with interlayer exciton energy. 4

Fig. 2 Logic and data flow of the adapted data-driven approach (i.e., *py*GWBSE) 6

Fig. 3 Structure models of the AB-stacked bilayer $MoSe_2$ and bilayer $MoSe_2/WSe_2$ heterostructure system..... 6

Fig. 4 Predicted band structures for the AB-stacked bilayer $MoSe_2$ system with PBE (red) and *GW* (blue) methods. The PBE predicted gap is 1.34 eV, which is corrected to 2.06 eV with the *GW* method..... 7

Fig. 5 Predicted band structure for the AB-stacked bilayer $MoSe_2/WSe_2$ heterostructure system. The direct gap (1.42 eV) is the energy difference between the conduction band (CB) and VB edges at K-point, whereas the indirect gap is the energy difference between the CB edge in between the K–Γ symmetry path and VB edge at K-point. The direct gap increases to 2.2 eV with QP-correction using the *GW* method. The experimental gap is 1.6 eV. 8

Fig. 6 Predicted frequency-dependent dielectric constants using the BSE method for the AB-stacked bilayer $MoSe_2$, bilayer WSe_2, and bilayer $MoSe_2/WSe_2$ heterostructure systems 9

Fig. 7 Micrograph with false coloring showing an hBN–WSe_2–hBN heterostructure stacked using a dry-transfer process 10

Fig. 8 STM surface images: (Left) naturally mined MoS_2 monolayer with many sulfur vacancies present; (Right) WSe_2 monolayer using UW-Madison's flux growth method and transfer process, with no visible defects in frame..... 11

Fig. 9 (Left) Micrograph of exfoliated monolayer $MoSe_2$ using a metal-assisted transfer process with approximate dimensions of 100 × 10 µm. (Right) Micrograph of exfoliated monolayer $MoSe_2$ using a metal-assisted transfer process with approximate dimensions of 10 × 10 µm. 12

Fig. 10 15- × 15-µm monolayer: (Left) Micrograph of TMD device before encapsulation. (Right) Zoomed-in micrograph of TMD device after hBN encapsulation. Residue has been removed from the device channel area but is still present on the edges of the contact pads. 13

Fig. 11 PL microscope with conjugate image planes for TMD studies 14

Fig. 12 (a) An optical microscopic image of the stacked $MoSe_2/WSe_2$ heterostructure sample from Professor Philip Kim's group at Harvard, with different stacked regions labeled and colored for clarity.

(b) Previous image of sample in PL apparatus with ~2-μm spot size superimposed. (c) New image of sample in apparatus with improved image quality and submicron beam spot size that results in better spatial resolution. Improvements in image clarity and resolution, and excitation laser spot size were primarily achieved through installation of a cryo-optic objective located inside the cryostat chamber. 14

Fig. 13 PL data for the stacked $MoSe_2/WSe_2$ heterostructure from Professor Philip Kim's group at Harvard over a range of temperatures (indicated in the legend upper right of each plot) and excitation power (indicated by the title of each column). Emission from the constituent WSe_2 and $MoSe_2$ monolayers is seen between 750 and 850 nm. Emission from the interlayer exciton of the coupled system is seen near 925 nm for all temperatures tested and most notably at room temperature (295 K).. 15

Fig. 14 IX in $MoSe_2/WSe_2$ heterostructure. (a) Temperature-dependent PL spectra in interlayer exciton (IX). Double-Lorentzian fits to the line shape indicate contributions from the IX (red lines) and IX^T, a three-carrier charged species. (b) Peak wavelength of IX and IX^T emission. (c) FWHM of IX and IX^T emission. 16

Fig. 15 Schematic of current PL mapping experimental setup to investigate interlayer exciton properties 17

Fig. 16 Temperature-dependent PL mapping of $Wse_2/MoSe_2$ heterostructures. (a–c) PL maps of the IX signal, filtered by a long-pass filter ($\lambda > 900$ μm), for a 10- × 10-μm area indicated by (d) the red box in the image of the $Wse_2/MoSe_2$ heterostructure. (e,f) Spectra taken at different temperatures at the location indicated by the red circles in (a,b)..... 18

Fig. 17 Analysis of temperature-dependent data of $WSe_2/MoSe_2$ heterostructure. (a) Temperature-dependent spectra of $WSe_2/MoSe_2$ heterostructure. (b) Spectrally integrated luminescence intensity ratio IX^T/IX vs. 1/temperature at the spot indicated by the red circle. (c) Integrated intensity of IX^T/IX and DX^T/DX from literature..... 19

Fig. 18 Before (left) and after (right) AFM images of $WSe_2/MoSe_2$ heterostructure with annealing and AFM processes applied. The black rectangle on the left indicates the squeegeed area. The sample has been annealed and undergone an AFM "squeegee" technique to clean sample interfaces, which can be seen by the rectangular border on the right. 20

Fig. 19 PL of "as-stacked" $MoSe_2/WSe_2$ heterostructure. (Left) Spectra at different spots across the sample at 4K. (Right) An optical image of the sample with circles indicating where measurements were made.. 20

Fig. 20 Model plexcitonic heterostructure. (b) Calculated scattering spectra as a function of gold (Au) nanocube size. (Reprinted with permission from Kuriakose and Nordlander, Rice University.)..... 21

Fig. 21 (a) Image of $MoSe_2$ monolayer, encapsulated in hBN, with relevant dimensions noted. (b) Dark-field image of nanocubes deposited on sample (SEM image of nanocube on right). (Reprinted with permission

from Hone, Columbia University.) (c) Scattering spectra from Au cubes off the TMD (black) and on the TMD (blue). The PL emisstion of TMD (red) overlaps with dip to indicate coupling. 22

Fig. 22 (a) Diagram of Au nanopillars for electron beam lithographic deposition. (b) Sample dark-field scattering spectra of a single 120-nm-diameter nanopillar. (c) Image of as-pattered Au nanopillars on TMD WSe_2 23

Fig. 23 (a) Temperature-dependent PL of unpatterned TMD and (b) 4K PL after Au nanoparticle deposition. The direct exciton is indicated via the green bar and the localized states are indicated via the blue bar. 24

Fig. 24 Materials scaling and device integration road map. (a) Approach to large area exfoliation in Professor Rhodes' group at UW-Madison. (b) Approach to MOCVD synthesis and large area scaling of 2D materials and devices. (Reprinted with permission from Professor Saptarshi Das, Pennsylvania State University.) 25

Fig. 25 ARL's 2D material-to-system integration road map 26

List of Tables

Table 1 Anticipated improvements of 2D-plexciton detectors over photomultiplier tube technology 2

Table 2 Predicted bandgaps using DFT and *GW* methods..... 8

Table 3 Predicted effective masses (m_e) for the AB-stacked bilayer $MoSe_2$, bilayer WSe_2, and $MoSe_2/WSe_2$ heterostructure 9

Table 4 Reported defect densities for various WSe_2 growth methods..... 11

1. Introduction

Advancements in sensing technologies, including sensitive high-speed photodetectors operating in the electromagnetic spectrum, directly benefit multi-domain operations across the defense and intelligence landscapes. Novel miniaturized sensors with reduced size, weight, and power (SWaP) are critical for on-board deployment on ground, flight, and space-based mobile platforms. As semiconductor technologies and traditional device architectures have been developed and optimized for decades, only incremental advances can be anticipated where existing methodologies are followed. Transformative new approaches must therefore be sought to overcome fundamental limitations associated with traditional bandgap materials.

Within this effort we target a fundamentally different approach to device design to advance capabilities beyond existing sensing platforms. We seek the development of foundational tools to realize a transformative, *tailorable* photodetector architecture with enhanced sensitivity by using hybrid 2D transition metal dichalcogenide (TMD)—plexcitonic (plasmon-excitonic) heterostructures—for detection across the near-infrared (NIR) spectral range with potential for room-temperature operation. This is accomplished by selecting TMD monolayers in heterogeneous stack configurations, guided by modeling of the coupled system, to tailor the spectral responses of intra- and interlayer excitons to the specific needs of an application space. Light–matter interactions are further enhanced using plasmonic arrays of metallic nanoparticles for the selected wavelength and temporal responses desired, and as a path to hyperspectral imaging.

We anticipate at least 1–2 orders-of-magnitude improvement over the state of the art (SOA) in spectral and temporal responses, sensor sensitivity, and signal-to-noise (S/N) ratio and SWaP requirements. Table 1 compares our expected advancement to the SOA in NIR spectroscopy photomultiplier tubes (PMTs). PMTs boast high sensitivities and low noise metrics by utilizing expensive cooling requirements and electronic gain. Additional comparisons can be made to room-temperature, low-SWaP IR detector technologies such as VO_2, where responsivities of approximately 0.5 mA/W with $D^* < 4 \times 10^9$ Jones[1] are observed with slow response times. For 2D-TMD-based detectors, we project gains in spectral and temporal response (<100 ps), sensor sensitivity (S/N; 10–100 A/W with $D^* > 10^{12}$ Jones[2,3]), and SWaP (<10-μW operating power), with additional modalities added in tailorable enhanced properties, tunable responses, electronic gating/control,[4] and directional detection. User-selectable efficiency, spectral responsivity, and bandwidth that break previous constraints on SWaP will enable advances in remote and autonomous sensing, miniaturized hyperspectral detection, optical communications with

directional control, and low-power integrated photonics within a highly customizable architecture.

Table 1 Anticipated improvements of 2D-plexciton detectors over photomultiplier tube technology

Attribute	SOA – PMT	2D-plexciton detector advancement
Focal plane mass (with front-end electronics)	500 gm 10-µm pixel pitch	<25 gm (integrated electronics) <5-µm pixel pitch (+ hyperspectral)
Response time (MCP-detector system)	>1 ns	10–100 ps (adjustable *and* gatable w/o loss of dynamic range)
Power consumption	7–12 W (cooling) ~1 kV (gain)	<10 µW (2D FET) <1 V (>10 A/W responsivity)

We assembled a diverse team across the US Army Combat Capabilities Development Command (DEVCOM) Army Research Laboratory (ARL), leveraging academic collaborators with expertise in 2D material synthesis and fabrication to accelerate progress. Together, the ARL team possesses key expertise in theoretical modeling for optimized device designs; material synthesis and characterization of film and interface quality; advanced spectroscopy and ultrafast characterization of exciton properties and phenomena; plasmonic enhancement and control of key device properties; and optoelectronic device design and benchmarking. Under the seedling tenure, we observed room-temperature existence of the interlayer exciton, demonstrating the *high-operating temperature* viability for this device platform, as well as resonant and spatially resolved optical excitations that implicate spectral responsivities. We progressed material maturation with focused, iterative studies of sample quality and lateral homogeneities that were carried out in close collaboration with sample fabrication and development. We demonstrated plasmonic coupling to TMD monolayers with synthetic nanoparticles, and initiated design and fabrication of nanoparticle arrays through scalable processes to target a path to manufacturability and detector arrays. These milestones help pave the path toward multifunctional arrays of TMD-plexciton pixels with targeted responses for next-generation sensing platforms to benefit National Security.

2. Project Overview

We seek the development of *foundational tools* for this fundamentally new class of optoelectronic device concepts based on hybrid 2D-plexcitonic devices. The effort's tasks were divided into two proof-of-concept thrusts:

1) Identify and optimize 2D TMDs layer stacks with the goal of controlling the excitonic properties (i.e., excited state lifetimes and absorption/emission spectra) that govern detector responses. Create correlations between the measurement of excitonic physics and band alignment effects with theoretical prediction and analysis, which is critical for our design-to-requirement vision.

2) Demonstrate plasmonic enhancement/coupling of metallic nanoparticles to excitons in monolayer TMDs encapsulated in hexagonal boron nitride (hBN). The control of excitonic properties in TMD layers through plasmonic interaction attempts to circumvent the gain-bandwidth product that has been considered an immutable property of most detector platforms.

Planned follow-on research will build off our program progress toward these goals, ultimately combining the two thrusts and integrating plasmonic nanoparticles with 2D-TMD layer stacks to demonstrate control of key properties for future devices with full control of the detector's spectral and temporal responses.

Our chosen platform of excitons in TMDs targets their unique electronic and optical properties for novel devices.[5,6] Excitons are bound electron hole pairs that mediate the light–matter interaction. They are charge neutral with high mobilities in TMDs, resulting in long transport distances with low losses. The extremely large exciton binding energies (0.4–0.9 eV)[7] in these 2D systems, widely tunable bandgaps (0.75–2+ eV) from visible to IR responsivity, and the resultant long lifetime of these species (>> 1 ns),[8] make them especially unique for optoelectronic applications. These properties, combined with extremely tunable material properties—based on interface design, heterogeneous stacking design, stacking angle control, and electric field modulation—provide a strong basis for building unique device architectures. The ability to design interfaces and stacking configurations, and accessible surface control through plasmonic coupling (see Fig. 1a), is especially unique for tailoring excitonic properties.

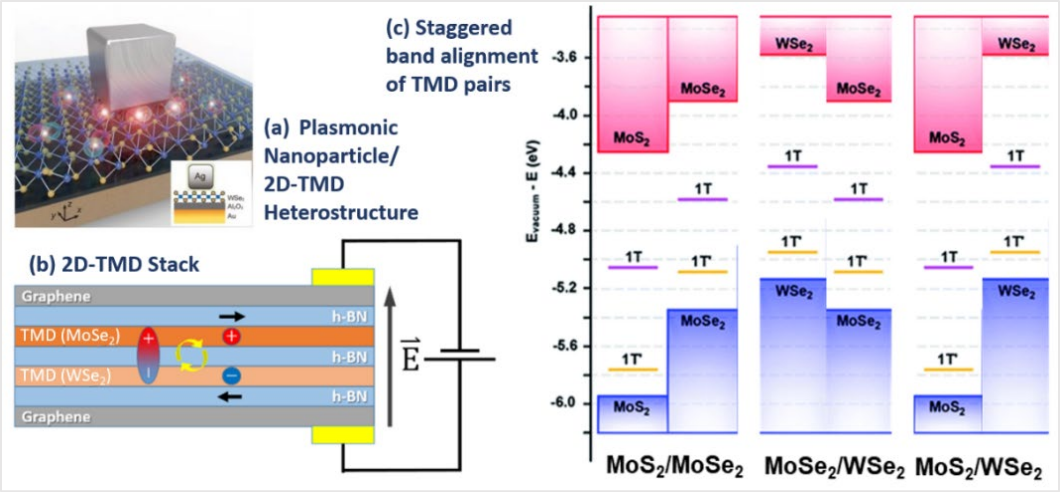

Fig. 1 (a) Plasmonic nanoparticle on TMD.[9] (b) Stacked TMD excitonic device. (c) Energy band diagram of targeted TMD layer stacks for three candidate heterostructures (adapted from Durán Retamal et al.[10]), chosen based on effective mass (m*) mismatch and staggered band alignment, with interlayer exciton energy.

Additionally, stacking well-selected TMD monolayer pairs, can lead to trapping carriers in separate layers (indirect or interlayer excitons), extending their lifetime, and can allow for the formation of exciton condensates and strongly correlated systems at near room temperatures.[11] This configuration occurs naturally in TMD heterostructures that have a type-II staggered band alignment. For example, in an $MoSe_2/WSe_2$ heterostructure (see Fig. 1b), the interlayer exciton comprises an electron in the conduction band of the $MoSe_2$ layer bound across the interface to a hole in the WSe_2 valence band; the energy spacing of that pairing results in luminescence at approximately 935 nm (1.35 eV). The interlayer exciton formation is very efficient due to the rapid (<50 fs) charge transfer process,[12] which is significantly faster than the intralayer exciton decay time. The fact that the electrons and holes are located across an interface gives rise to an out-of-plane electric dipole whose properties can be tuned by varying the interlayer distance and/or applying an external electric field along the dipole axis. For instance, transient absorption spectroscopy measurements show the hole transfer time in the interlayer exciton formation process increases by 3 orders of magnitude when inserting a 1-nm hBN layer between $MoSe_2$ and WSe_2 monolayers.[13] The energy of the interlayer exciton may be varied further with a tuning range of approximately 80–138 meV by applying an external electric field perpendicular to the surface.[14]

The model guiding our material selection and heterostructure design considers two TMD layers that are separated by varying thicknesses of the hBN layers, which act as a dielectric spacer layer. Calculations are based on a first-principal theory coupled with an effective-mass-based variational principle for excitonic properties[15]; additional detail is given in Section 3.

TMD layer combinations are carefully chosen to provide a staggered band alignment to assist in the formation of interlayer excitons, along with large electron/hole effective masses and perfectly nested Fermi surfaces (momentum/effective mass matching). Using these criteria, we have three TMD layer combinations for investigation (band diagram in Fig. 1c): $MoS_2/MoSe_2$, MoS_2/WS_2, and $MoSe_2/WSe_2$. Due to material quality considerations and available materials, we focused our attention on $MoSe_2/WSe_2$. An overview of material considerations is presented in Section 4, and spectroscopic studies and analysis of these materials is discussed in Section 5. Plasmonic-nanoparticle/TMD pairings are guided by electromagnetic simulations to ensure relevant spectral overlap; additional detail is given in Section 6. We conclude with an outlook on current and future directions for 2D material research and development in Section 7.

3. Modeling of Excitons in TMDs

To understand the role of heterogeneity and its resultant proximal effects on the TMD layers, we have performed band structure calculations of the 2D homo- and heterostructure systems using both the basic first-principles method and the more rigorous many body perturbation theory (MBPT) within the Green's function/screened Coulombic interaction (*GW*) approximation as implemented in the Vienna Ab initio Simulation Package (VASP) tool. The open-source software code *py*GWBSE[16] was used to automatically converge important parameters such as the number of bands. In the MBPT + *GW* formalism, the quasi-particle (QP) energies are calculated by calculating the first-order perturbative correction to the Kohn–Sham (KS) eigenvalues by approximating self-energy as a product of one particle Green's function (*G*) and screened Coulomb interaction (*W*). Partial self-consistency was implemented by allowing the number of iterations in *G* to increase until bandgap convergence within 0.1 eV was reached (GW_0). It has been shown that MBPT within the *GW* approximation is particularly useful in computing QP properties for a wide variety of semiconductors and insulators without requiring any ad hoc introduction of mixing parameters like those needed for hybrid functionals used in density functional theory (DFT).[17] A complete flowchart of the *py*GWBSE framework is presented in Fig. 2.

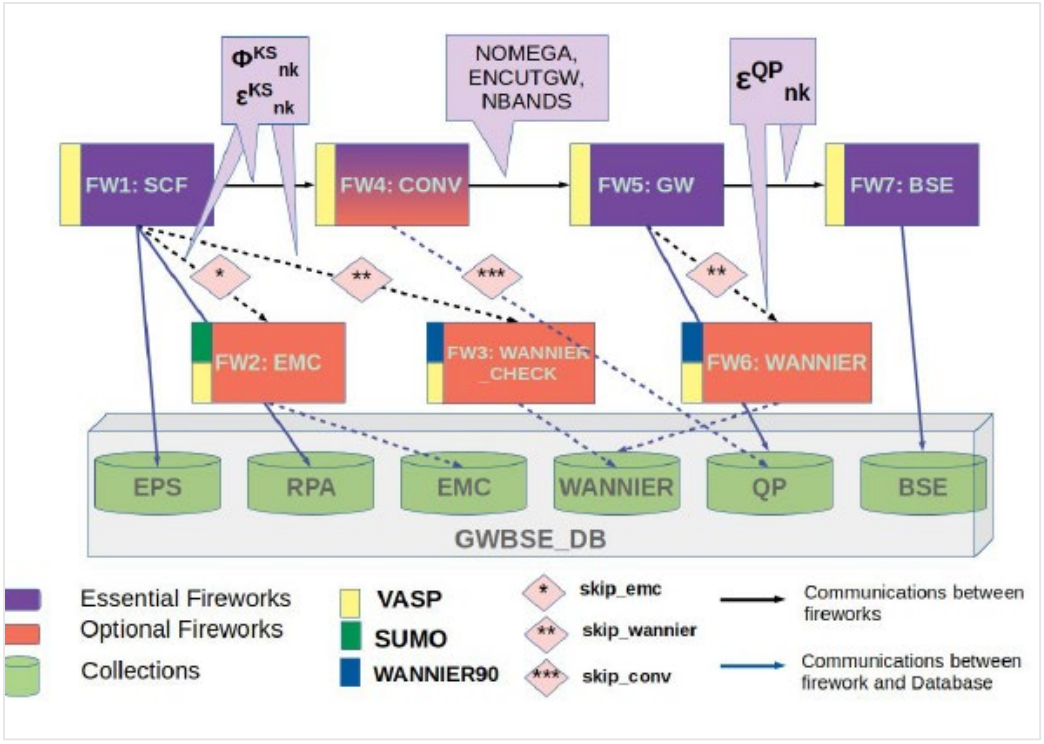

Fig. 2 Logic and data flow of the adapted data-driven approach (i.e., *py*GWBSE[16])

For this project, we have considered the AB-stacked $MoSe_2$ bilayer, WSe_2 bilayer, and $MoSe_2/WSe_2$ bilayer heterostructure systems. The structural models of the $MoSe_2$ bilayer and $MoSe_2/WSe_2$ bilayer systems are illustrated in Fig. 3.

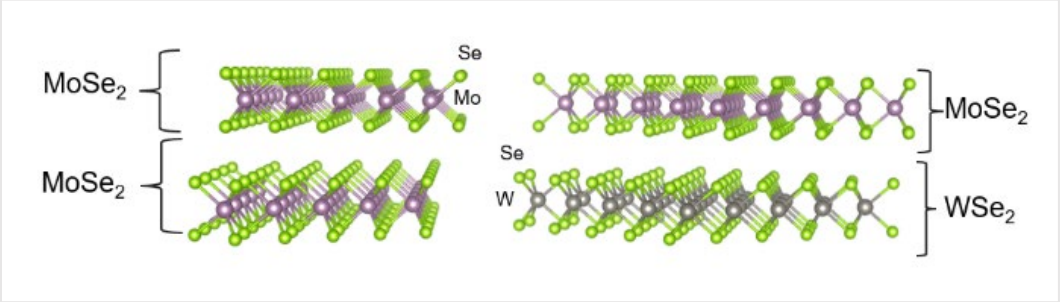

Fig. 3 Structure models of the AB-stacked bilayer $MoSe_2$ and bilayer $MoSe_2/WSe_2$ heterostructure system

To highlight the importance of the correct bandgap prediction, the predicted band structures from both the conventional Perdew–Burke–Ernzerhof (PBE) functionals and *GW* method—a Green's function-based method in which the self-energy correction to the QP interaction is implemented by calculating the product of the single-particle Green function *G* and the screened interaction *W* for the bilayer $MoSe_2$ system (Fig. 4). Quantitatively, the PBE functional predicts the fundamental bandgap of 1.38 eV for the bilayer $MoSe_2$ system, which is 40% less than the

experimentally observed gap for the same system. However, due to the correction to the self-energy error and inclusion of the MBPT, the predicted bandgap from the *GW* approximation is 2.06 eV, which is close to the experimental value reported in the literature.

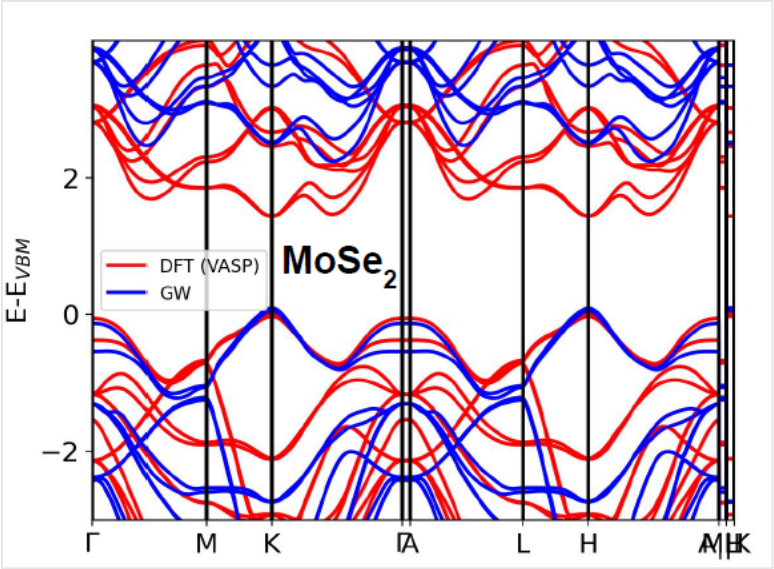

Fig. 4 Predicted band structures for the AB-stacked bilayer $MoSe_2$ system with PBE (red) and *GW* (blue) methods. The PBE predicted gap is 1.34 eV, which is corrected to 2.06 eV with the *GW* method.

The calculated QP band structure for the $MoSe_2/WSe_2$ bilayer system is presented in Fig. 5. The predicted bandgap using the single-particle PBE is 1.12. The *GW* correction results in a 1.78-eV bandgap—an increase of 45% over the PBE method, which is consistent with previous theoretical work[18] that reported a bandgap of 1.67 eV. The *GW* bandgap of 1.78 eV in $MoSe_2/WSe_2$ is slightly higher than that of AB-stacked WSe_2 (1.80 eV), and higher than AB-stacked $MoSe_2$ (1.62 eV). A comparison of the DFT and *GW* predicted gaps is summarized in Table 2. Based on analysis of the element-resolved band structures, we observed that the valence band maxima (VBM) states originate from the WSe_2 layer, whereas the conduction band minima (CBM) states are mainly composed of states from the $MoSe_2$ layer. Since the WSe_2 valence band (VB) edge states are above the $MoSe_2$ VB edge states, the initial state of the hole transfer occurs between the layers through the delocalization of the VB states, facilitating ultrafast charge transfer across the weakly coupled vdW heterostructure. The instantaneous hole transfer is ultrafast and independent of temperature because of the thermodynamically supported charge transfer across the vdW gap. Experimental validation of the observed charge dynamics in these heterostructures is planned.

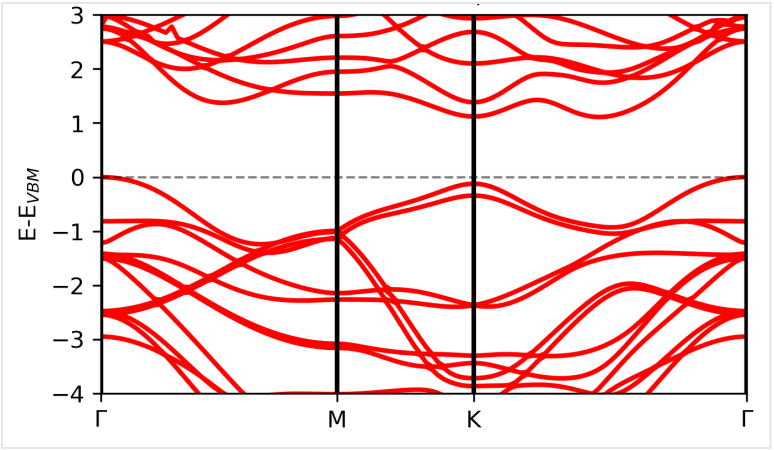

Fig. 5 Predicted band structure for the AB-stacked bilayer $MoSe_2/WSe_2$ heterostructure system. The direct gap (1.42 eV) is the energy difference between the conduction band (CB) and VB edges at K-point, whereas the indirect gap is the energy difference between the CB edge in between the K–Γ symmetry path and VB edge at K-point. The direct gap increases to 2.2 eV with QP-correction using the *GW* method. The experimental gap is 1.6 eV.

Table 2 Predicted bandgaps using DFT and *GW* methods

Bilayer material	DFT gap	DFT gap (direct)	*GW* gap	*GW* gap (direct)
$MoSe_2$	1.38	1.55	2.06	2.35
WSe_2	1.64	1.75	2.32	2.63
$MoSe_2 + WSe_2$	1.35	1.42	2.20	2.50

Since the carrier effective masses are critical material-specific parameters that define excitonic binding energy and Bohr radius, an accurate prediction of the electron and hole effective masses was performed by analyzing the band structure and performing parabolic fits to the band edges using the sumo tool,[19] which is integrated in the *py*GWBSE framework. In all cases, the VBM is located at Γ. For the $MoSe_2$ on WSe_2 heterostructure, the hole effective mass $m_{eff,h}$ was found isotropic with the value of 1.07 m_e in both the Γ-to-M and Γ-to-K directions, which closer to the average value between the $MoSe_2$ (1.12 m_e) and WSe_2 (1.00 m_e) electron masses.

In all structures considered, the CBM is located between Γ and K. Since the band dispersions in these systems exhibit anisotropic behavior and lead to nonhomogeneous charge and carrier mobilities, we have analyzed effective masses along the [100] direction (i.e., Γ–K path), and the [010] direction (i.e., Γ–M path), for all the systems. The extracted electron effective masses ($m_{eff,e}$) for the $MoSe_2$ on WSe_2 heterostructure along the [100] and [010] directions are 0.70 and 0.43 m_e, respectively. This contrasts with the bilayer $MoSe_2$ system, which has relatively smaller effective masses along the [100] and [010] directions (i.e., 0.54 and 0.56

m_e, respectively). Additionally, we find that the [100] and [010] electron masses for the bilayer WSe_2 are closer to that of the bilayer $MoSe_2$ system with values of 0.54 and 0.50 m_e, respectively. The results from our effective mass calculations are summarized in Table 3.

Table 3 Predicted effective masses (m_e) for the AB-stacked bilayer $MoSe_2$, bilayer WSe_2, and $MoSe_2/WSe_2$ heterostructure

System	Electron		Hole
$MoSe_2/MoSe_2$	0.54 (Γ–K)	0.56 (Γ–M)	1.12
WSe_2/WSe_2	0.54 (Γ–K)	0.52 (Γ–M)	1.00
$MoSe_2/WSe_2$	0.70 (Γ–K)	0.43 (Γ–K)	1.07

At the DFT level, we calculate the static dielectric constant tensor, which gives us the in-plane ($\varepsilon_\parallel$) and out-of-plane ($\varepsilon_\perp$) dielectric constants. The $MoSe_2/WSe_2$ system sees $\varepsilon_\parallel = 9.44\ \varepsilon_0$ and $\varepsilon_\perp = 15.80\ \varepsilon_0$, which is between the $MoSe_2$ structure ($\varepsilon_\parallel = 9.74\ \varepsilon_0$ and $\varepsilon_\perp = 16.58\ \varepsilon_0$) and the WSe_2 structure ($\varepsilon_\parallel = 9.11\ \varepsilon_0$ and $\varepsilon_\perp = 15.01\ \varepsilon_0$).

Additionally, by solving the Bethe–Salpeter equation (BSE), we also predicted the frequency-dependent dielectric constants for all the analyzed systems (Fig. 6).

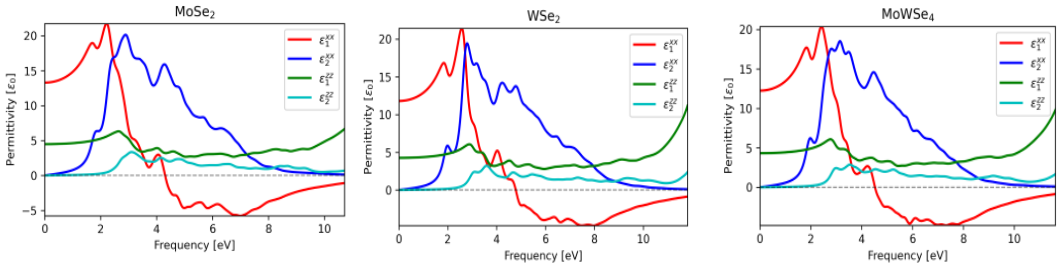

Fig. 1 Predicted frequency-dependent dielectric constants using the BSE method for the AB-stacked bilayer $MoSe_2$, bilayer WSe_2, and bilayer $MoSe_2/WSe_2$ heterostructure systems

4. Material Development

TMDs were sourced from university collaborators at Harvard University, Columbia University, and the University of Wisconsin-Madison (UW-Madison), where atomically thin monolayers of TMDs are controllably exfoliated from flux-grown bulk crystals.[20] Our collaborators in Professor Daniel Rhodes' group at UW-Madison use traditional scotch-tape exfoliation and metal-assisted exfoliation methods to cleave monolayers of TMDs from bulk crystals.[21] A polycarbonate-based dry-transfer process is used for stacking atomically thin van der Waals crystals to create heterostructures.[22] A micrograph of a stacked TMD heterostructure is presented in Fig. 7.

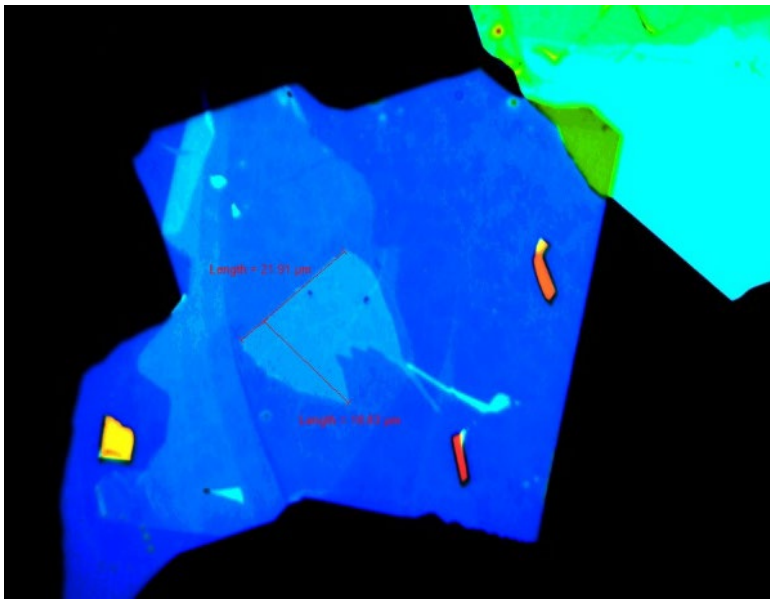

Fig. 2 Micrograph with false coloring showing an hBN–WSe_2–hBN heterostructure stacked using a dry-transfer process

There are several reported methods for growing TMD crystals such as WSe_2. Methods for growing bulk crystals with relatively high crystal uniformity include chemical vapor transport (CVT) and flux transport. Methods for growing thin film crystals down to individual monolayers include chemical vapor deposition (CVD) and molecular beam epitaxy (MBE). Defect densities vary greatly by growth method, but based on the published literature, the materials sourced from the Rhodes Group at UW-Madison were able to produce WSe_2 bulk crystals that had 4,000-times-fewer defects than CVD-grown WSe_2, and 100-times-fewer defects than MBE or CVT-grown WSe_2. Figure 8 shows a scanning tunneling microscope (STM) image comparing a naturally mined TMD with a flux-grown TMD using the process developed at UW-Madison. Table 4 compiles literature results as compared to their flux-grown crystals.

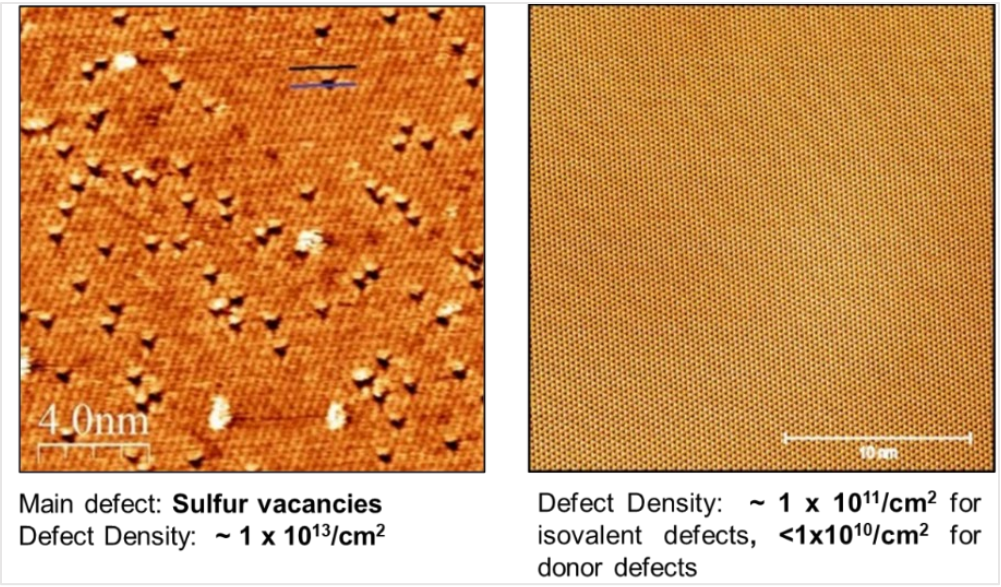

Fig. 3 STM surface images: (Left) naturally mined MoS_2 monolayer with many sulfur vacancies present; (Right) WSe_2 monolayer using UW-Madison's flux growth method and transfer process, with no visible defects in frame

Table 2 Reported defect densities for various WSe_2 growth methods

WSe_2 growth method	Defect density (cm^{-2})
CVD	$4.7 \pm 0.3 \times 10^{13}$ cm^{-2} [22]
MBE	$2.8 \pm 0.3 \times 10^{12}$ cm^{-2} [23]
CVT 1	2.22×10^{12} cm^{-2} [24]
CVT 2	1.22×10^{12} cm^{-2} [25]
CVT 3	$1.1 \pm 0.3 \times 10^{12}$ cm^{-2} [26]
ARL/UofW CVT	5.2×10^{12} cm^{-2}
UofW Flux	**1×10^{10} cm^{-2}**

The following major challenges need to be addressed regarding synthesis of large-area, atomically thin TMDs: material defects, strain, grain boundaries, and surface impurities. Processing introduces additional contaminants and defects that must be mitigated to ensure that material properties are maintained and not degraded during device and structure fabrication. Stamping methods are being developed by ARL collaborators to create a repeatable process of placing monolayer TMDs with areas in the 10s of microns with low defect densities. To address the challenge of material defects and grain boundaries, UW-Madison developed a flux growth method that has produced some of the highest-quality bulk TMD crystals reported in the literature. We maintain investment in these processes by funding and overseeing the research of two graduate students in the Rhodes Group's lab at UW-Madison.

Strain, edge boundaries, and point defects are being addressed through improvements in the metal-assisted and dry-transfer processes being used for exfoliating and stacking monolayer van der Waals materials. These materials reduce or eliminate the use of harsh chemical processing and polymer contact with the TMD, which cause point defects and contamination. There are several experiments and optimizations in the works to maintain low defect densities in the TMD monolayers, while also improving edge boundaries and pattern repeatability of the stamped 2D materials. Figure 9 provides a micrograph of transferred $MoSe_2$ rectangular and square areas with dimensions ranging from 10 to 100 µm. Methods for improving yield and minimizing edge boundary tearing are also being developed—including thermal cycling methods, directional control of exfoliation along Burgers vectors, and modification of the SiO_2 substrate adhesion with the TMD. Additionally, methods to remove residues from the transfer process and device fabrication are being developed. The force of encapsulating devices and TMD stacks using hBN has shown promise for pushing out residues. Physical removal of residues is also being explored using nanoprobes to push debris and residues out of target areas (or nano-squeegeeing, discussed in Section 5). An example TMD device that had residue removed with hBN encapsulation is shown in Fig. 10.

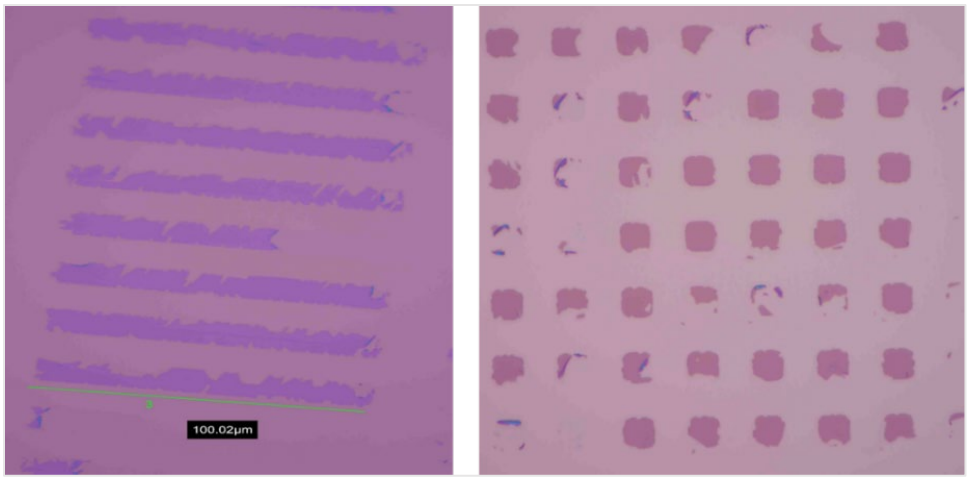

Fig. 9 (Left) Micrograph of exfoliated monolayer $MoSe_2$ using a metal-assisted transfer process with approximate dimensions of 100 × 10 µm. (Right) Micrograph of exfoliated monolayer $MoSe_2$ using a metal-assisted transfer process with approximate dimensions of 10 × 10 µm.

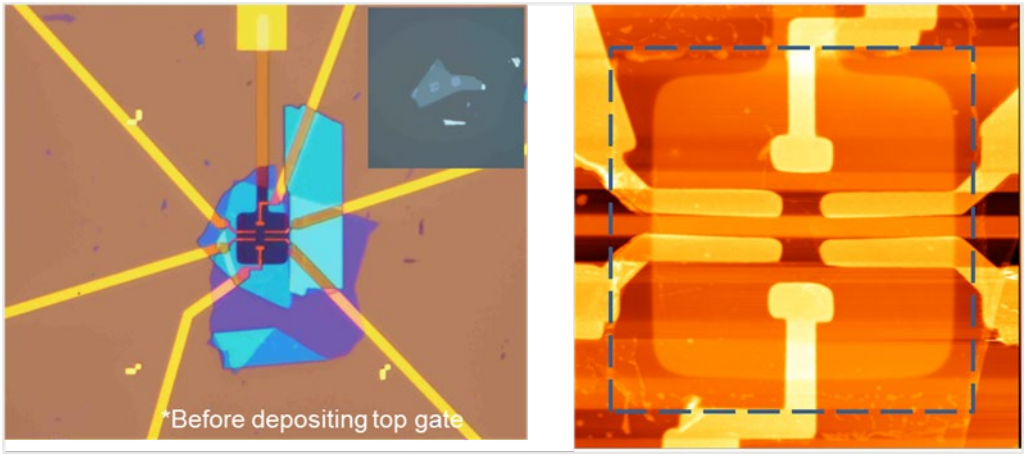

Fig. 10 15- × 15-µm monolayer: (Left) Micrograph of TMD device before encapsulation. (Right) Zoomed-in micrograph of TMD device after hBN encapsulation. Residue has been removed from the device channel area but is still present on the edges of the contact pads.

5. Spectroscopy and TMD Analysis

Due to the small scale of high-quality TMD monolayers and heterostructure stacks, it was necessary to modify our spectroscopic equipment at ARL, which had previously been used to study large-area semiconductor thin films for optoelectronic applications. For photoluminescence (PL) measurements of stacked structures, we designed and built a compact setup with conjugate image planes to align laser excitation and collection of emission with relevant sample features; the sample is mounted in a low-vibration closed-cycle cryostat (4–300 K) for temperature control. The optical apparatus, shown in Fig. 11 (without the cryostat), consists of three arms (from left to right): a path for the incoming laser beam, a path to image the sample, and a path to excite the sample and collect the outgoing light. The setup sits on an *xyz*-stage that allows for measurements on different regions on the sample by moving the excitation and collection components in concert. Additional improvements included the installation of an intrachamber cryogenic optical module (cryo-optic) that places the microscope objective in the cryostat vacuum chamber and alleviates optical aberrations that are otherwise introduced by imaging through cryostat windows. This has directly led to improved imaging quality and resolution in our system, as seen in the comparison between a previously acquired image in Fig. 12b with an improved image from the updated setup in Fig. 12c. We also installed a sample nanopositioner in the cryostat for precise control of sample movements and three-axis positioning, and later a laser scanner (discussed below). These key steps allowed us to easily distinguish between different sample features and achieve precise sample positioning, as well as reduce the laser spot size to submicron (from ~2 µm, previously). Reducing the beam spot size helps to ensure the excitation/emission region is confined to selected

locations in the heterostructure sample and proved important for 2D mapping of sample characteristics as we sought to improve sample homogeneities.

Fig. 11 PL microscope with conjugate image planes for TMD studies

Fig. 12 (a) An optical microscopic image of the stacked $MoSe_2/WSe_2$ heterostructure sample from Professor Philip Kim's group at Harvard, with different stacked regions labeled and colored for clarity. (b) Previous image of sample in PL apparatus with ~2-μm spot size superimposed. (c) New image of sample in apparatus with improved image quality and submicron beam spot size that results in better spatial resolution. Improvements in image clarity and resolution, and excitation laser spot size were primarily achieved through installation of a cryo-optic objective located inside the cryostat chamber.

Figure 13 plots PL data acquired on the stacked $MoSe_2/WSe_2$ heterostructure shown in Fig. 12, which was performed as a function of temperature at different excitation powers. Spectral features of note are (from shorter-to-longer wavelength): emission from the constituent WSe_2 and $MoSe_2$ monolayers between 700 and 850 nm; and emission from the interlayer exciton of the coupled

heterostructure near 925 nm. We observed emission from the interlayer exciton at all temperatures studied, notably with detectable emission *at room temperature*. This particular observation is essential to our long-term goal of achieving lightweight NIR/IR detectors, making it possible to exploit interlayer exciton properties at elevated temperatures without the need for expensive cryo-cooling.

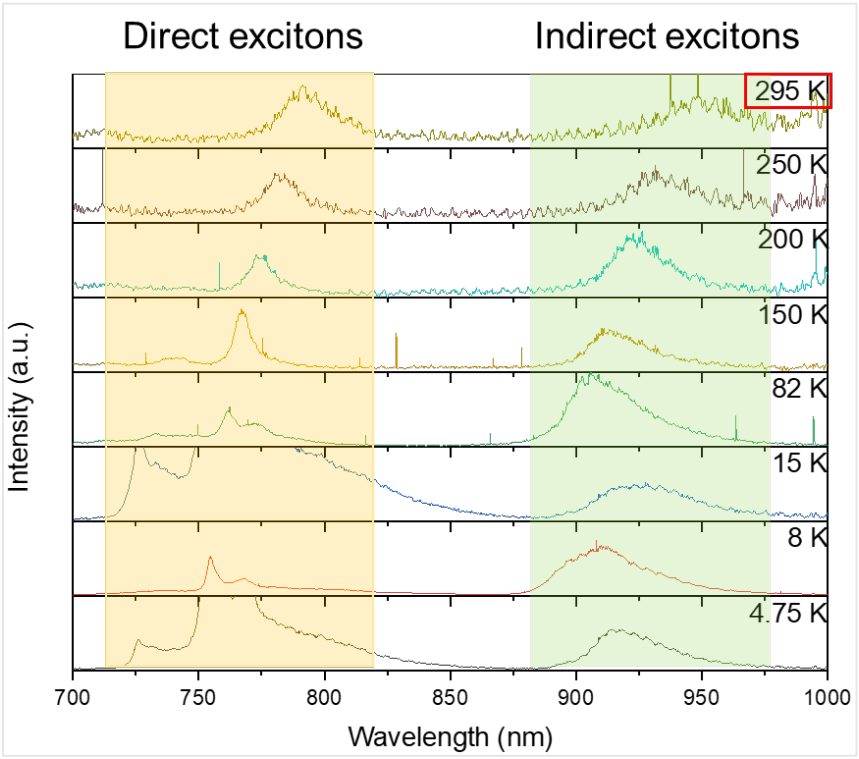

Fig. 13 PL data for the stacked $MoSe_2/WSe_2$ heterostructure from Professor Philip Kim's group at Harvard over a range of temperatures (indicated in the legend upper right of each plot) and excitation power (indicated by the title of each column). Emission from the constituent WSe_2 and $MoSe_2$ monolayers is seen between 750 and 850 nm. Emission from the interlayer exciton of the coupled system is seen near 925 nm for all temperatures tested and most notably at room temperature (295 K).

We performed additional analyses of the interlayer exciton emission as a function of temperature to better understand the complex tunneling formation and recombination processes that govern device efficiencies. Figure 14 plots emission spectra (Fig. 14a) with double-Lorentzian fits to represent the interlayer, indirect exciton (IX), and indirect trion (IX^T: a three-carrier, charged species) populations that are present. The peak wavelength and full-width half-maximum (FWHM) of these fits are plotted in Fig. 14b and 14c, respectively. Although care was taken to probe the same spatial location, we see significant variation in peak position and width due to inhomogeneities; however, the relative intensities of the IX and IX^T also vary significantly. It is expected that in a uniform film the peak wavelength of the IX emission will decrease as the temperature decreases, which is not observed

here. This is clearly due to inhomogeneities present in the sample. Excitons in TMDs have strong Coulomb interactions and hence are very susceptible to their local environment (defects, stress, etc.). We then refined our scanning capabilities further to enable 2D PL mapping to characterize such inhomogeneity and improve our fabrication process for a more homogeneous response. As experimental parameters are changed (e.g., temperature), the sample in the cryostat may move; thus, making it difficult to characterize the exact spot again. To fully understand the complex interplay of different species and their dynamics, full temperature and power dependencies are crucial.

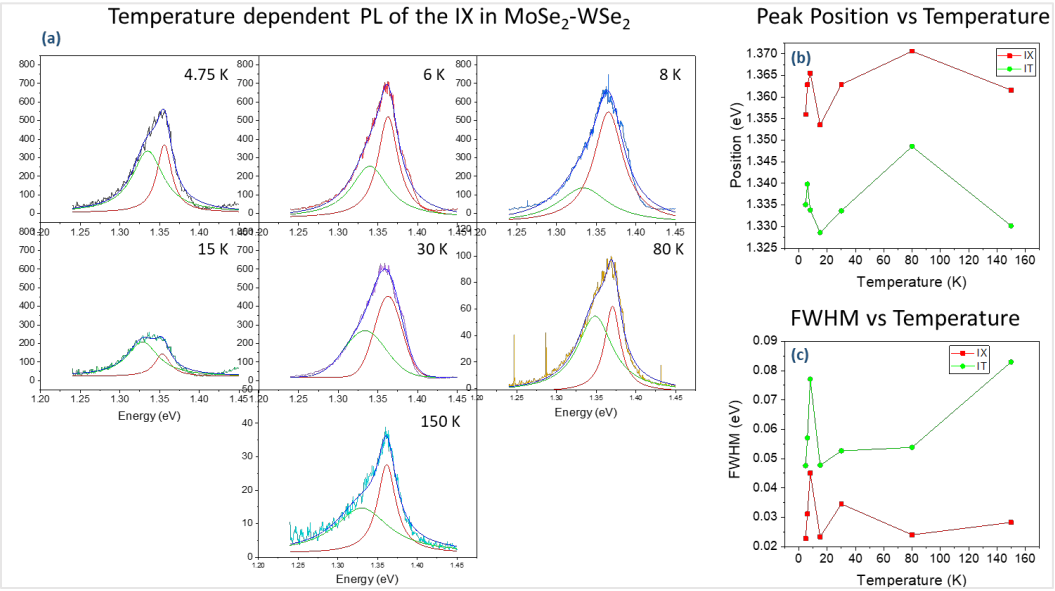

Fig. 14 IX in $MoSe_2/WSe_2$ heterostructure. (a) Temperature-dependent PL spectra in interlayer exciton (IX). Double-Lorentzian fits to the line shape indicate contributions from the IX (red lines) and IX^T, a three-carrier charged species. (b) Peak wavelength of IX and IX^T emission. (c) FWHM of IX and IX^T emission.

Figure 15 is a schematic of our current advanced micro-PL setup with precise mapping capability. The system scans the beam across an area of the sample and registers the collected PL to its corresponding position. This is a 4*f* optical imaging system in which the beam spot on the image plane (indicated in Fig. 15) is imaged to the focal plane of the objective (at the sample). A galvanometer driven mirror, which is used to steer the beam, is placed at the back focal plane of the scanning lens (f_2 away). This plane is conjugate with the entrance aperture (Fourier plane) of the objective lens to ensure efficient collection to the sample. As the mirror rotates, the beam spot at the image plane moves latterly on the sample while maintaining the beam entrance through the aperture of the objective (only the angle through that aperture changes). The specifications of the optics are chosen to select a specific

beam magnification (spot size), so that the laser beam spot on the sample is diffraction limited.

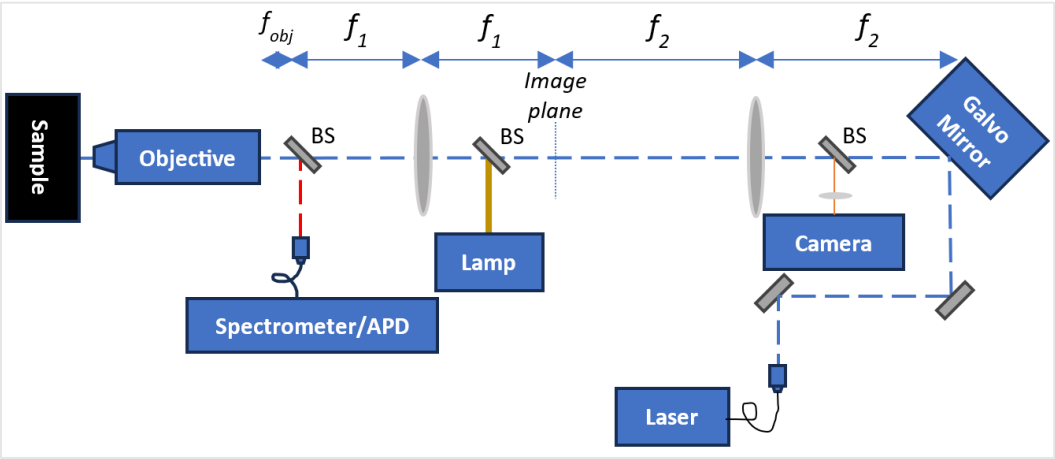

Fig. 15 Schematic of current PL mapping experimental setup to investigate interlayer exciton properties

Figure 16 shows temperature-dependent PL data on a $WSe_2/MoSe_2$ heterostructure obtained by the PL mapping setup described above. Figure 16a–16c are PL maps of a 10- × 10-um area (shown in Fig. 16d) filtered through a long-pass filter to target the interlayer exciton ($\lambda > 900$ μm). Note the high resolution of the images—this is due to the diffraction limited beam spot. This capability provides a way to locate and interrogate particular spots/areas with greater accuracy. For example, we can identify a "hot spot" and/or homogenous area on the sample and trace it as experimental parameters and conditions are varied (e.g., as the temperature is changed). Furthermore, we can track a particular spot/area on a sample as the positioning varies. Figure 16e and 16f showcase this feature. Figure 16e and 16f show representative spectra for a series of temperatures (indicated in the legend) taken with defocused and focused beam spots from the locations (shown in Fig. 16a and 16b, respectively). We note an improvement in our dataset, as compared to previous results shown in Fig. 13. The spectra show a consistent trend as the temperature changes. This will enable temperature-dependent analysis of the underlying recombination mechanisms as data is captured from a consistent sample location.

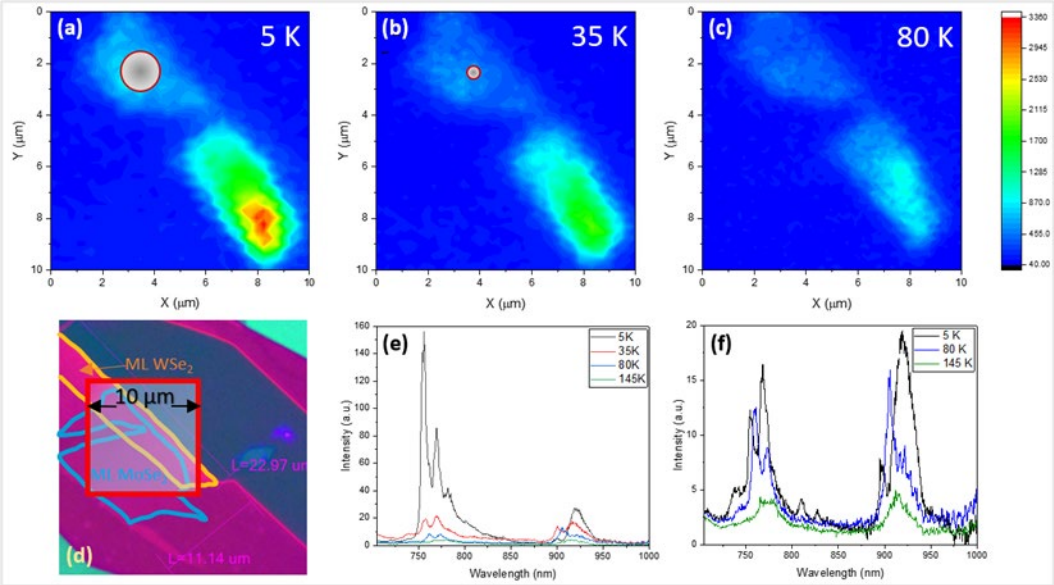

Fig. 16 Temperature-dependent PL mapping of $Wse_2/MoSe_2$ heterostructures. (a–c) PL maps of the IX signal, filtered by a long-pass filter (λ > 900 μm), for a 10- × 10-μm area indicated by (d) the red box in the image of the $Wse_2/MoSe_2$ heterostructure. (e,f) Spectra taken at different temperatures at the location indicated by the red circles in (a,b).

Figure 17a is a stacked plot of Fig. 16e of the representative spectra. Two lines of indirect luminescence can be observed near 900 nm. The lower (higher) energy peak was ascribed to a charged (neutral) interlayer exciton.[27] Such assignment was made because the luminescence intensity ratio of the IX^T/IX lines decrease with increasing temperature (Fig. 17c and 17d). We compared our data (Fig. 17b) and found it consistent with the literature. This gives us confidence in our PL mapping capability to track important material properties including carrier lifetimes, different species population densities, absorption/emission spectra, etc., which directly implicate device parameters and performance.

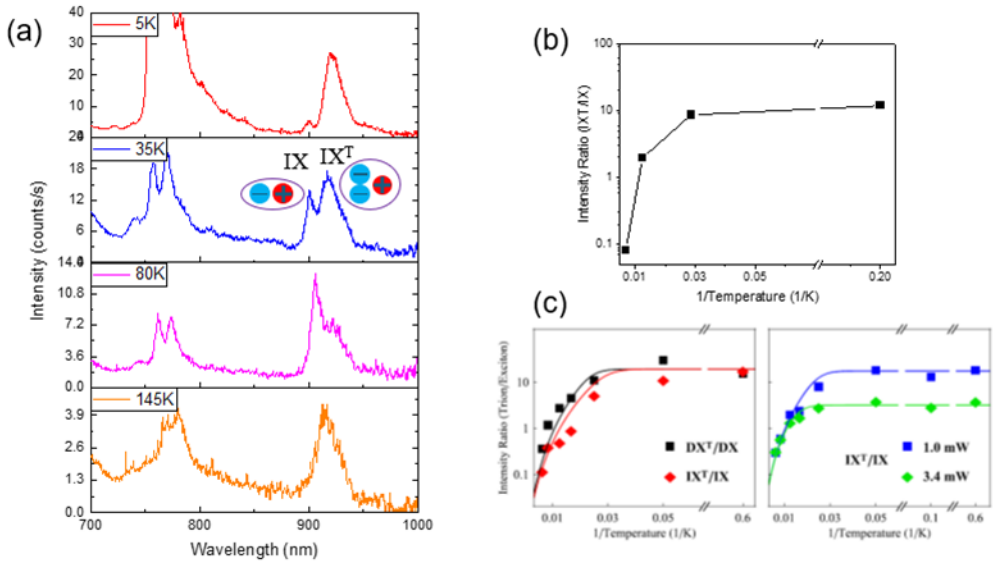

Fig. 17 Analysis of temperature-dependent data of $WSe_2/MoSe_2$ heterostructure. (a) Temperature-dependent spectra of $WSe_2/MoSe_2$ heterostructure. (b) Spectrally integrated luminescence intensity ratio IX^T/IX vs. 1/temperature at the spot indicated by the red circle. (c) Integrated intensity of IX^T/IX and DX^T/DX from literature.[27]

To improve sample uniformities in stacked TMD_x–TMD_y heterostructures, we initiated annealing and atomic force microscope (AFM) "squeegeeing" studies, in an iterative controlled procedure. Thermal annealing of encapsulated TMD monolayers at high temperatures is expected to improve sample quality, most notably the stability and optical properties.[28,29] Heterostructure samples can then be cleaned using an AFM tip to controllably squeeze, or squeegee, out contaminates (from reactants generated during processing and stacking procedures) and nanobubbles causing nonuniformities at the interface.[30] We applied annealing procedures to hBN-encapsulated heterostructure stacks at 250 °C under vacuum for 1 h. The top hBN layer in a heterostructure stack of $MoSe_2/WSe_2$ was then cleaned with the AFM squeegee technique. PL measurements from our first attempt revealed no signal from the interlayer exciton, indicating potential damage from the AFM tip. After confirming the existence of the interlayer exciton of a new sample (not shown), we proceeded to anneal the sample at 250 °C for 1 h, then cleaned part of the sample using an AFM tip (squeegee). Figure 18 shows AFM images of the heterostructure sample before and after annealing and squeegeeing. The PL results from this sample (Fig. 19) show an improvement of the interlayer exciton signal on the squeegeed area (spots 2–4), as compared to the non-squeegeed area (spot 1), an encouraging result for future progress. We are currently improving our fabrication technique by iterating through the process described above to observe the effect individual steps have on sample emissions (i.e., quality).

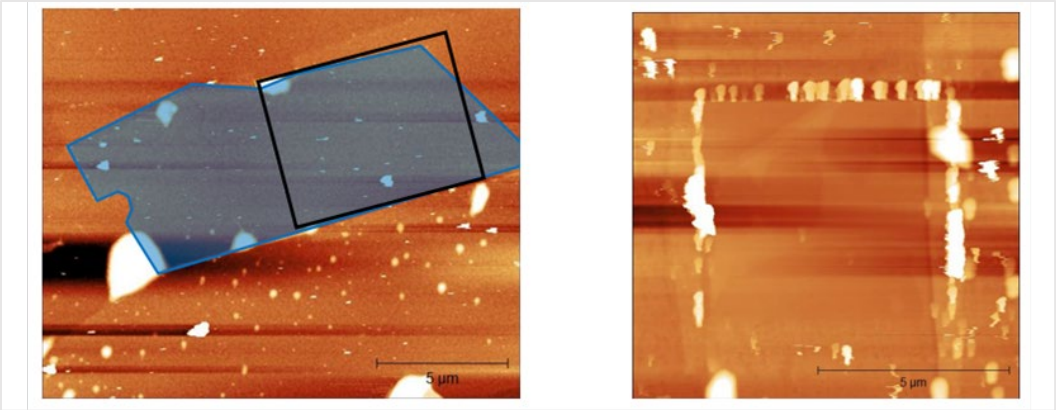

Fig. 18 Before (left) and after (right) AFM images of $WSe_2/MoSe_2$ heterostructure with annealing and AFM processes applied. The black rectangle on the left indicates the squeegeed area. The sample has been annealed and undergone an AFM "squeegee" technique to clean sample interfaces, which can be seen by the rectangular border on the right.

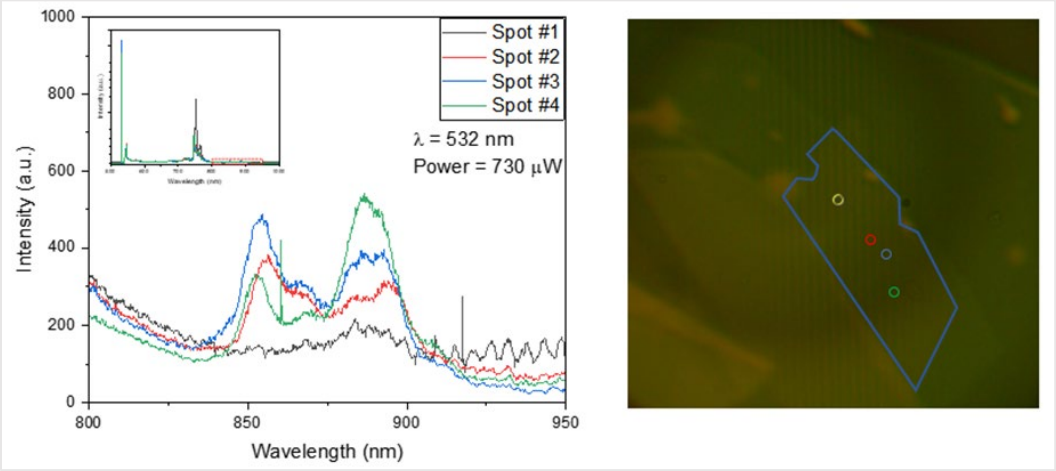

Fig. 19 PL of "as-stacked" $MoSe_2/WSe_2$ heterostructure. (Left) Spectra at different spots across the sample at 4K. (Right) An optical image of the sample with circles indicating where measurements were made.

6. Plasmonic Coupling to TMDs

The localized surface plasmon resonance (LSPR) is the coherent oscillation of electrons in the presence of an electric field within a nanoparticle. This resonance wavelength is highly dependent on the nanoparticle's material, size, shape, and local dielectric environment. Understanding and engineering the LSPR for a specific wavelength continues to gain attention due to the large electric field enhancement that occurs around nanoparticles. Previous work has used nanomaterial's LSPR to enhance a TMD's optical properties. For instance, Wang et al.[9] engineered a TMD/plasmonic heterostructure that produced a 20,000-fold enhancement of the PL emission from WSe_2. A key component of this enhancement

is the coupling between the LSPR and the exciton of the TMD forming a new QP, a plexciton. Plexciton formation requires spectral overlap between the LSPR and the TMD's exciton. This can present a challenge due to the LSPR's relationship to the local environment. Factors such as the substrate choice or hBN layer thickness can red- or blue-shift the LSPR out of being spectrally overlapped with the exciton.[31] To help anticipate these challenges, we partnered with Professor Peter Norlander of Rice University to perform finite-difference time-domain (FDTD) calculations of the plexcitonic heterostructure.

We used FDTD calculations to simulate the scattering spectra of nanoparticles with different local environments. By altering parameters such as substrate, particle size, and particle material, we predicted which nanoparticles will produce an LSPR that overlaps with the exciton energy. We also simulated what effect the exciton would have on the LSPR. As shown in Zheng et al.,[31] when there is coupling between the exciton and the LSPR, Rabi splitting is observed in both the simulated and experimental data. Using this framework, we modeled different plexcitonic device configurations to predict which arrangement would be optimal for coupling. From the FDTD calculations we determined 90-nm gold cubes placed on $MoSe_2$ encapsulated in hBN on a Si/SiO_2 substrate would produce a plexcitonic heterostructure, as shown in Fig. 20.

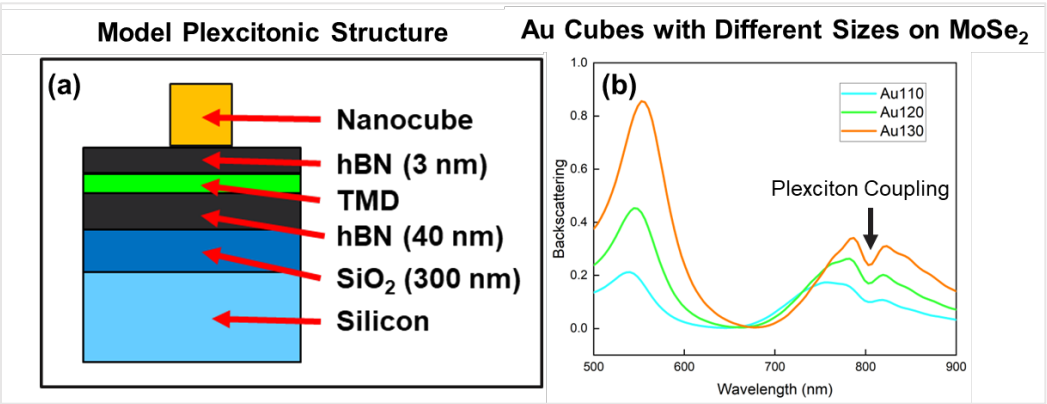

Fig. 20 Model plexcitonic heterostructure. (b) Calculated scattering spectra as a function of gold (Au) nanocube size. (Reprinted with permission from Kuriakose and Nordlander, Rice University.)

To fabricate this device, we partnered with Columbia University's Professor James Hone to produce the encapsulated $MoSe_2$, where a thin <5-µm hBN layer was used to encapsulate the TMD while still providing the necessary proximity to the $MoSe_2$ monolayer to enable coupling (shown in Fig. 21a with layer dimensions noted). The 90-nm gold nanoparticles (cubes) were purchased from Nanopartz (Fig. 21b, right side). To apply the nanoparticles to the encapsulated TMD, a series of spin-coating and drop-casting procedures were performed until nanomaterial was observed on

the area of interest. Successfully deposited nanoparticles are shown in Fig. 21b (circled in yellow). Dark-field scattering spectra were then performed to confirm the presence of splitting in the spectra, shown in Fig. 21c. The black curve shows the scattering spectra of an isolated Au cube on the Si/SiO_2 surface. The blue curve shows the scattering spectra of an isolated Au cube on the Si/SiO_2 surface. The blue curve shows the scattering spectra of one specific Au cube on the encapsulated TMD. The shift in the LSPR center frequency is due to the change in the local environment around the cube. Furthermore, a splitting in the spectrum can be seen at approximately 780 nm. This overlaps with PL emission from the TMD exciton, shown in red. Based on the results shown in Fig. 21, we have generated a plexciton structure between the TMD and the Au nanocube. Ideally, the LSPR would be centered over the exciton emission. Deviations are due in part to the cube measuring less than the stated 90 nm (as seen via scanning electron microscopy [SEM]), shifting the LSPR to a lower wavelength.

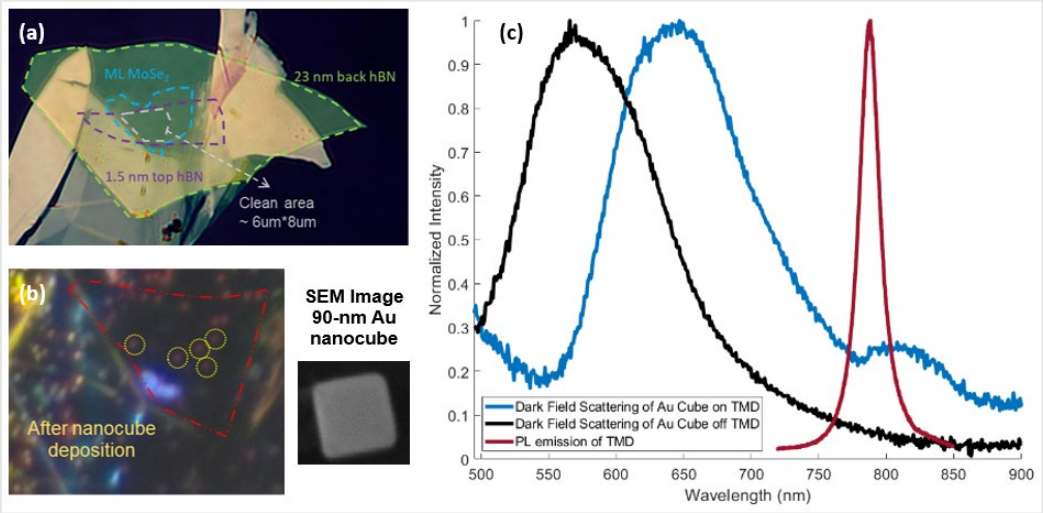

Fig. 21 (a) Image of $MoSe_2$ monolayer, encapsulated in hBN, with relevant dimensions noted. (b) Dark-field image of nanocubes deposited on sample (SEM image of nanocube on right). (Reprinted with permission from Hone, Columbia University.) (c) Scattering spectra from Au cubes off the TMD (black) and on the TMD (blue). The PL emisstion of TMD (red) overlaps with dip to indicate coupling.

To pursue scalable processes, we initiated fabrication of plasmonic nanopillar arrays using electron-beam lithography. Drop casting suspended synthetic nanoparticles onto a sample is an unreliable and uncontrollable means of achieving spatial overlap. We therefore worked to optimize our lithographic techniques to apply plasmonic material and LSPR spectral properties. Like the synthetic nanocube approach, heterostructure design was vetted using FDTD calculation to confirm the size and type of metal that would produce an LSPR that overlaps with the TMD's exciton. Based on the FDTD calculations, the fabrication process

targeted Au pillars with diameters between 70 and 150 nm, a height of 50 nm, and 1-µm spacings to target modeled parameters (shown in Fig. 22a). After iterating our procedure, we deposited Au nanopillars onto encapsulated WSe_2 with 120- and 140-nm diameters. Dark-field scattering spectra (see Fig. 22b) performed on these nanopillars confirmed the general spectral overlap with WSe_2 exciton emission. Figure 22c is an image of nanopillar arrays patterned directly onto an encapsulated WSe_2 monolayer.

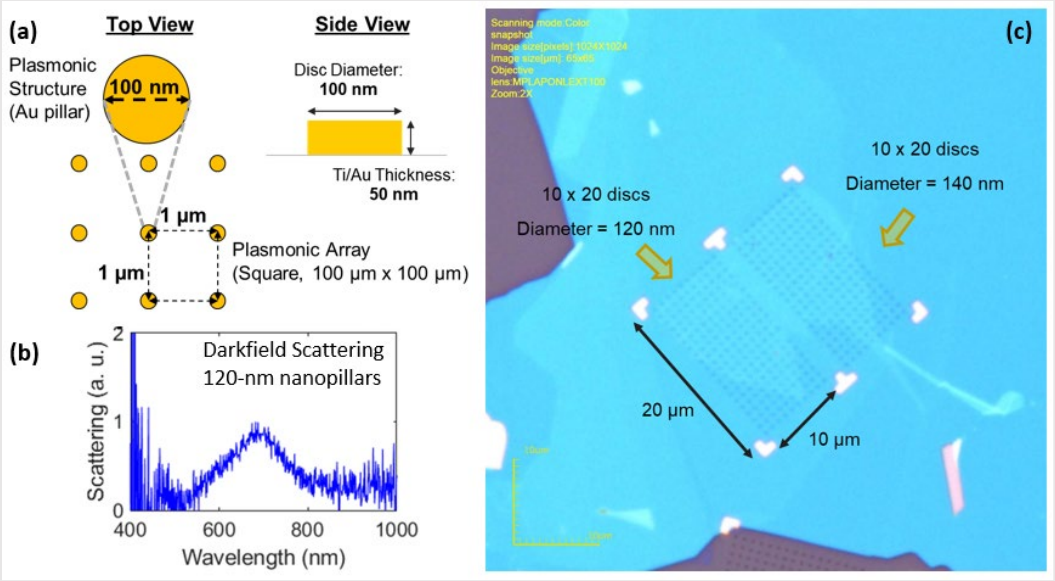

Fig. 22 (a) Diagram of Au nanopillars for electron beam lithographic deposition. (b) Sample dark-field scattering spectra of a single 120-nm-diameter nanopillar. (c) Image of as-pattered Au nanopillars on TMD WSe_2.

Maps of PL emission were generated before and after nanopillar deposition with the aim of observing optical enhancement/modification of the PL emission. Spectra from these maps are shown in Fig. 23. Figure 23a shows the effect temperature has on encapsulated WSe_2 prior to deposition. As the sample temperature decreases, emission from spectral features that are generally associated with localized states can be detected. After deposition, the magnitude of these localized states increases dramatically, as shown in Fig. 23b. This increase could be due to the introduction of new defects or an enhancement of existing localized states. Currently, we are investigating different lithography techniques to understand the source of the observed effects, prevent the formation/enhancement of localized states, and instead enhance the exciton emission.

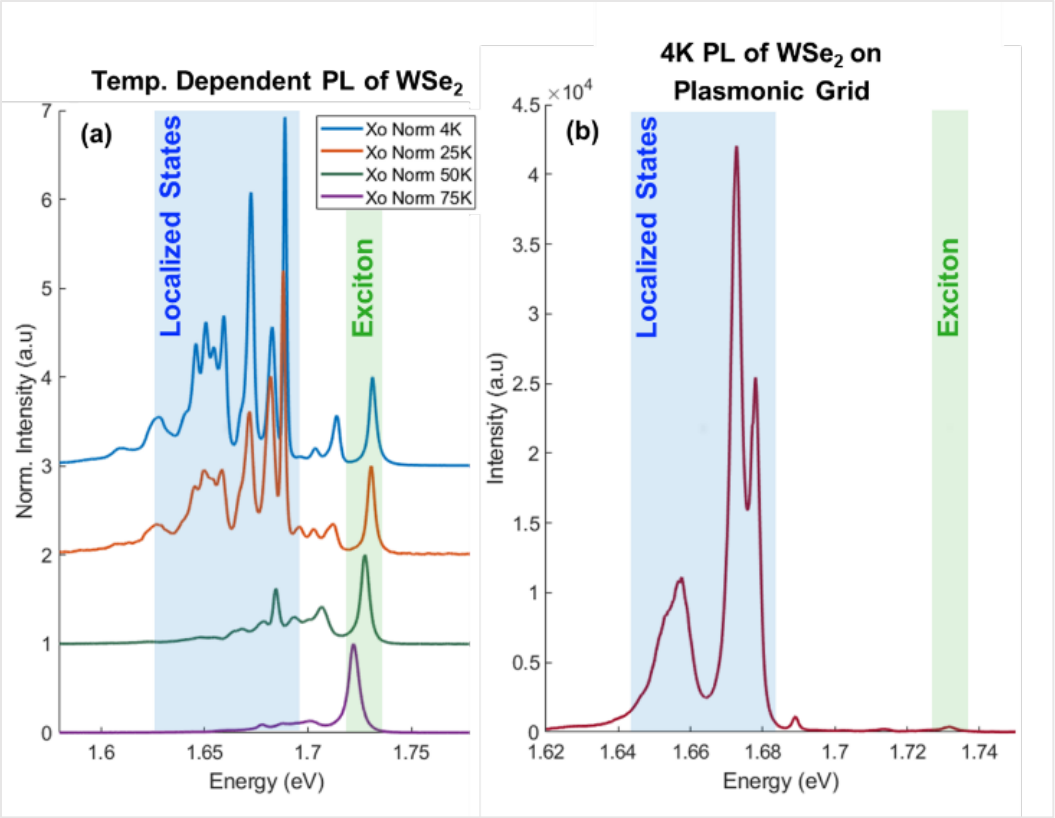

Fig. 23 (a) Temperature-dependent PL of unpatterned TMD and (b) 4K PL after Au nanoparticle deposition. The direct exciton is indicated via the green bar and the localized states are indicated via the blue bar.

7. Conclusion: ARL's 2D Material-to-System Integration Roadmap

In this effort, we focused on demonstrating the unique properties of 2D materials and their heterostructures. The rich emission characteristics that 2D materials possess, with exotic low-energy emissions of interlayer excitons that are observed even at room temperature, along with strong plasmonic interactions in our results, highlight the exotic light–matter interactions in 2D materials that can be leveraged for fundamentally different optoelectronic device architectures. These findings strongly suggest that 2D materials and their van der Waals heterostructures have great potential to create new opportunities for development of compact designer detectors. However, there are two main barriers for these laboratory demonstrations to find their way into applications: 1) achieving large-scale quality material with required uniformity for integration and 2) establishing large-scale integration and device-fabrication processes.

The ARL team built external partnerships with leading academic and industry experts to assemble a research community that aims to solve the issues of material manufacturability, device scaling, and integration (see Fig. 24). With several internal activities focused on assembly and optimization of 2D-based optoelectronic devices[32–35] we have set the stage to develop arrays of 2D-based photodetectors and integrate them to read out complementary metal-oxide semiconductor chips. This allows us to prototype and test some unique functionalities we have studied in this program in devices and system-level integration (Fig. 25). Our partnership with UW-Madison has led to a research activity to develop back-end-of-line compatible stamping and stacking techniques that transfer and place high-quality, large-area materials on any chip/substrate. In this interaction, we are dedicated to stimulating the discovery of best practices for material synthesis and device fabrication through collaborative efforts with Professor Rhodes' research group, with a focus toward integrating talent into the ARL team. We have also forged critical partnerships with Pennsylvania State University's 2D teams on metal-organic chemical vapor deposition (MOCVD) synthesis of 2D materials to scale and integrate devices for large-array prototyping and testing. Our efforts are being integrated into existing internal activities, with a focus on developing efficient processing and read-out circuitries. In particular, we have chips in design and fabrication where devices can be integrated into developing cognitive near-sensor platforms.

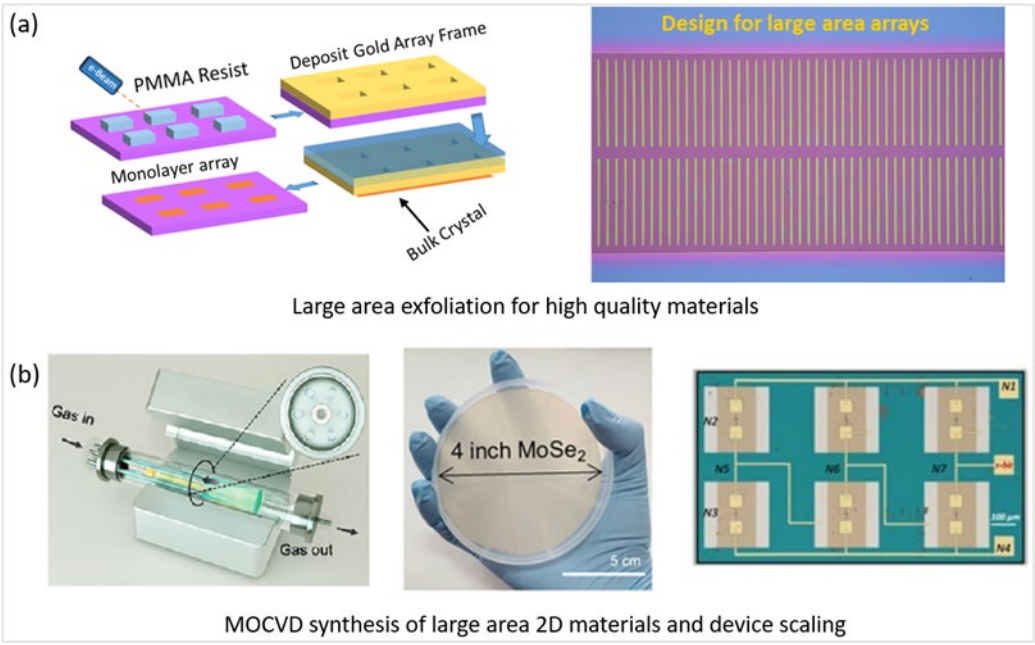

Fig. 24 Materials scaling and device integration road map. (a) Approach to large area exfoliation in Professor Rhodes' group at UW-Madison. (b) Approach to MOCVD synthesis and large area scaling of 2D materials and devices. (Reprinted with permission from Professor Saptarshi Das, Pennsylvania State University.)

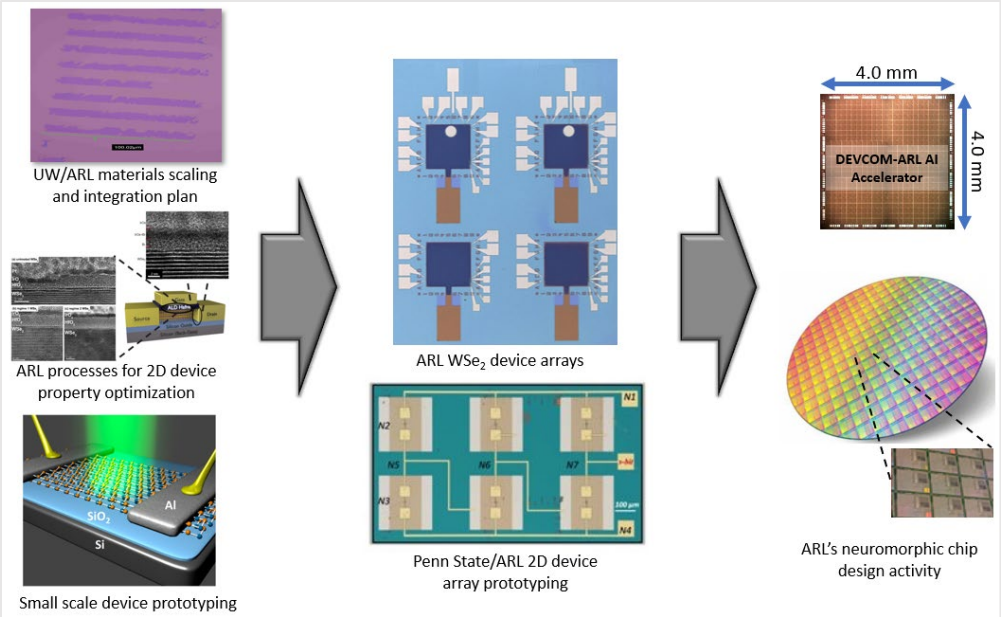

Fig. 25 ARL's 2D material-to-system integration road map

8. References

1. Xu D, Zhu X, An J, Chen G, Bao J, Xu X. UV-vis-IR broad spectral photodetectors based on VO(2)-ZnO nanocrystal films. ACS Omega. 2022;7(42):37078–37084.
2. Ross JS. Rivera P, Schaibley J, Lee-Wong E, Yu H, Taniguchi T, Watanabe K, Yan J, Mandrus D, Cobden D. Interlayer exciton optoelectronics in a 2D heterostructure p-n junction. Nano Lett. 2017;17(2):638–643.
3. Huo N, Konstantatos G. Recent progress and future prospects of 2D-based photodetectors. Adv Mater. 2018;30:e1801164.
4. Yang M, Ren L, Robert C, Tuan DV, Lombez L, Urbaszek B, Marie X, Dery H. Relaxation and darkening of excitonic complexes in electrostatically doped monolayer WSe2: roles of exciton-electron and trion-electron interactions. Phys Rev B. 2022;105:085302.
5. Basov DN, Fogler MM, Garcia de Abajo FJ. Polaritons in van der Waals materials. Science. 2016;354.
6. Wang Q, Lai J, Sun D. Review of photo response in semiconductor transition metal dichalcogenides based photosensitive devices. Opt Mater Express. 2016;6.
7. Palummo M, Bernardi M, Grossman JC. Exciton radiative lifetimes in two-dimensional transition metal dichalcogenides. Nano Lett. 2015;15:2794–2800.
8. Wang Z, Rhodes DA, Watanabe K, Taniguchi T, Hone JC, Shan J, Mak KF. Evidence of high-temperature exciton condensation in two-dimensional atomic double layers. Nature. 2019;574(7776):76–80.
9. Wang Z, Dong Z, Gu Y, Chang Y-H, Zhang L, Li L-J, Zhao W, Eda G, Zhang W, Grinblat G. Giant photoluminescence enhancement in tungsten-diselenide-gold plasmonic hybrid structures. Nat Commun. 2016;7(11283).
10. Durán Retamal JR, Periyanagounder D, Ke JJ, Tsai ML, He JH. Charge carrier injection and transport engineering in two-dimensional transition metal dichalcogenides. Chem Sci. 2018;9:7727–7745.
11. Calman EV, Fogler MM, Butov LV, Hu S, Mishchenko A, Geim AK. Indirect excitons in van der Waals heterostructures at room temperature. Nat Commun. 2018;9(1895).

12. Hong X, Kim J, Shi S-F, Zhang Y, Jin C, Sun Y, Tongay S, Wu J, Zhang Y, Wang F. Ultrafast charge transfer in atomically thin MoS(2)/WS(2) heterostructures. Nat Nanotechnol. 2014;9:682–686.

13. Yoon Y, Zhang Z, Qi R, Joe AY, Sailus R, Watanabe K, Taniguchi T, Tongay S, Wang F. Charge transfer dynamics in MoSe(2)/hBN/WSe(2) heterostructures. Nano Lett. 2022;22(24):10140–10146.

14. Zhang L, Zhang Z, Wu F, Wang D, Gogna R, Hou S, Watanabe K, Taniguchi T, Kulkarni K, Kuo T, et al. Twist-angle dependence of Moire excitons in WS(2)/MoSe(2) heterobilayers. Nat Commun. 2020;11(5888).

15. Debnath B, Barlas Y, Wickramaratne D, Neupane MR, Lake RK. Exciton condensate in bilayer transition metal dichalcogenides: strong coupling regime. Phys Rev B. 2017;96.

16. Biswas T, Singh AK. pyGWBSE: a high throughput workflow package for GW-BSE calculations. Npj Comput Mater. 2023;9.

17. Biswas T, Singh AK. Excitonic effects in absorption spectra of carbon dioxide reduction photocatalysts. NPJ Comput Mater. 2021;7.

18. Debbichi L, Eriksson O, Lebègue S. Electronic structure of two-dimensional transition metal dichalcogenide bilayers from ab initio theory. Phys Rev B. 2014;89.

19. Ganose AM, Jackson AJ, Scanlon DO. Sumo: command-line tools for plotting and analysis of periodic ab initio calculations. J Open Source Softw. 2018;3.

20. Edelberg D, Rhodes D, Kerelsky A, Kim B, Wang J, Zangiabadi A, Kim C, Abhinandan A, Ardelean J, Scully M, et al. Approaching the intrinsic limit in transition metal diselenides via point defect control. Nano Lett. 2019;19:4371–4379.

21. Li Z, Ren L, Wang S, Huang X, Li Q, Lu Z, Ding, S Deng H, Chen P, Lin J, et al. Dry exfoliation of large-area 2D monolayer and heterostructure arrays. ACS Nano. 2021;15(8):13839–13846.

22. Zhang S, Ugeda MM, Jin C, Shi S-F, Bradley AJ, Martín-Recio A, Ryu H, Kim J, Tang S, Kim Y, et al. Defect structure of localized excitons in a WSe_2 monolayer. Phys Rev Lett. 2017;119:046101.

23. Zhang Y, Ugeda MM, Jin C, Shi S-F, Bradley AJ, Martín-Recio A, Ryu H, Kim J, Tang S, Kim Y, et al. Electronic structure, surface doping, and optical response in epitaxial WSe_2 thin films. Nano Lett. 2016;16(4):2485–2491.

24. Amani M, Taheri P, Addou R, Ahn GH, Kiriya D, Lien D-H, Ager JW 3rd, Wallace RM, Javey A. Recombination kinetics and effects of superacid treatment in sulfur- and selenium-based transition metal dichalcogenides. Nano Lett. 2016;16(4):2786–2791.

25. Addou R, Wallace RM. Surface analysis of WSe(2) crystals: spatial and electronic variability. ACS Appl Mater Interfaces. 2016;8:26400–26406.

26. Yankowitz M, McKenzie D, LeRoy BJ. Local spectroscopic characterization of spin and layer polarization in WSe_2. Phys Rev Lett. 2015;115.

27. Calman EV, Fowler-Gerace LH , Choksy DJ , Butov LV, Nikonov DE , Young IA, Hu S, Mishchenko A, Geim AK. Indirect excitons and trions in MoSe(2)/WSe(2) van der Waals heterostructures. Nano Lett. 2020;20(3):1869–1875.

28. Hua X, Axenie T, Navarro Goldaraz M, Kang K, Yang E-H, Watanabe K, Taniguchi T, Hone J, Kim B, Herman IP. Improving the optical quality of MoSe(2) and WS(2) monolayers with complete h-BN encapsulation by high-temperature annealing. ACS Appl Mater Interfaces. 2022;14:2255–2262.

29. Cao Y, Wood S, Richheimer F, Blakesley J, Young RJ, Castro FA. Enhancing and quantifying spatial homogeneity in monolayer WS(2). Sci Rep. 2021;11;14831.

30. Rosenberger MR, Chuang H-J, McCreary KM, Hanbicki AT, Sivaram SV, Jonker BT. Nano-"squeegee" for the creation of clean 2D material interfaces. ACS Appl Mater Interfaces. 2018;10;10379–10387.

31. Zheng D, Zhang S, Deng Q, Kang M, Nordlander P, Xu H. Manipulating coherent plasmon-exciton interaction in a single silver nanorod on monolayer WSe(2). Nano Lett. 2017;17(6):3809–3814.

32. Hu J, Zhou F, Wang J, Cui F, Quan W, Zhang Y. Chemical vapor deposition syntheses of wafer-scale 2D transition metal dichalcogenide films toward next-generation integrated circuits related applications. Adv Funct Mater. 2023;33(40):2303520.

33. Mazzoni A, Burke R, Chin M, Najmaei S, Dubey M, Goldsman N, Daniels K. Comparison of contact metals evaporated onto monolayer molybdenum disulfide. J Appl Phys. 2022;132.

34. Sales MG, Mazzoni A, Sarney WL, Leff AC, Pearson J, Najmaei S, McDonnell S. Effects of atmospheric UV-O3 exposure of WSe_2 on the properties of the HfO_2/WSe_2 interface. Appl Phys Lett. 2023;123: 123502.

35. Sarney W, Glassman A, Pearson J, McGinn C, Litwin P, Singh Bisht R, Ramanathan S, McDonnell S, Hacker C, et al. Monolithic integration and ferroelectric phase evolution of hafnium zirconium oxide in 2D neuromorphic synaptic devices. Mater Today Nano. 2024;24.

List of Symbols, Abbreviations, and Acronyms

2D	two-dimensional
AFM	atomic force microscopy
ARL	Army Research Laboratory
Au	gold
BSE	Bethe–Salpeter equation
CB	conduction band
CBM	conduction band minimum
CVD	chemical vapor deposition
CVT	chemical vapor transport
DEVCOM	US Army Combat Capabilities Development Command
DFT	density functional theory
FDTD	finite-difference time-domain
FWHM	full-width half-maximum
GW	Green's function/screened Coulombic interaction
hBN	hexagonal boron nitride
IR	infrared
IX	indirect exciton
IX^T	indirect trion
KS	Kohn–Sham
LSPR	localized surface plasmon resonance
MBE	molecular-bean epitaxy
MBPT	many body perturbation theory
MOCVD	metal-organic chemical vapor deposition
$MoSe_2$	molybdenum diselenide
NIR	near infrared
PL	photoluminescence

PMT	photomultiplier tube
QP	quasi-particle
SEM	scanning electron microscopy
Si	silicon
SiO_2	silicon dioxide
S/N	signal-to-noise (ratio)
SOA	state of the art
STM	scanning tunneling microscope
SWaP	size, weight, and power
TMD	transition metal dichalcogenide
VASP	Vienna Ab initio Simulation Package
VB	valence band
VBM	valance band maximum
WSe_2	tungsten diselenide

1 (PDF)	DEFENSE TECHNICAL INFORMATION CTR DTIC OCA
1 (PDF)	DEVCOM ARL FCDD RLB CI TECH LIB